

# Self-shaping free-form spatial structure with large-deformable bunched CFRP rods

Peng Feng<sup>\*</sup>, Jiacheng Zhao, Qinyu Wang, Jiaqi Zhai, Peizhao Zhou

Department of Civil Engineering, Tsinghua University, Beijing 10084, China

## ARTICLE INFO

### Keywords:

Bending active  
Self-shaping system  
Large deformation theory  
Inverse form-finding calculation method  
Free-form spatial structure

## ABSTRACT

Based on the bending-active concept, this paper presents a self-shaping system with bunched carbon fiber-reinforced polymer (CFRP) rods to construct curved surfaces, establishing an overall design and construction process. Such component consists of a bunch of slender and easily bendable CFRP rods that are pre-formed and then bounded by connecting joints. Then, those components form free-form spatial structures. The proposed system offers several advantages: strong designability, low transportation cost, short construction period, polished appearance and low maintenance requirements during service. For component design, to determine the shape of such component, a two-stage mechanical analysis is proposed based on the large deformation theory and finite element analysis (FEA): a form-finding process to determine the deformed component shape through its cross-sections and boundary-load conditions; and a reverse form-finding process to obtain these above-mentioned parameters from a given component shape. The reliability of both methods is verified through in-plane bending tests. A design demonstration of a saddle-shaped curved spatial structure is performed using this method. Overall, the proposed system can guide the actual construction projects of complex curved surfaces with self-shaping bunched CFRP rods.

## 1. Introduction

Free-form spatial structures, characterized by double-curved surfaces, have emerged as a new generation of space-frame structures, offering architectural freedom and creativity beyond traditional geometric shapes [1]. Advancements in computer technology have facilitated their practical application, enabling rich architectural expression and impactful visual designs. These structures are commonly found in large-span buildings such as museums, libraries, sports venues, and mosques. Large-span free-form spatial structures can be classified into two categories based on their construction methods: cast-in-place and prefabricated. Cast-in-place structures are usually constructed by pouring concrete into specially shaped formwork on-site, resulting in longer construction time and higher cost. On the other hand, prefabricated structures involve preparing components in a factory and then transporting them to the site for assembly. Prefabrication offers convenience, reduced construction time, and environmental benefits. One notable prefabrication-based method for constructing free-form spatial structures is bending-active technology.

“Bending active” is a term commonly used to describe bent beams or free-form structures whose geometric shapes are achieved through elastic deformation from initially straight or flat components, such as rods, cables, and flexible membranes [2]. Typically, in normal prefabricated engineering projects, components usually need to be processed into specific shapes beforehand to form a spatial structure with minimal internal stress considering self-weight other than other loads. Unlike traditional prefabrication methods that require pre-bent components, bending-active concept allows for on-site bending of components to achieve the desired shapes. Hence, the components can be transported compactly to the construction sites and bent manually or mechanically to transform into pre-designed shapes automatically.

The application of bending-active concept in large-span spatial structures can be traced back to the 1970s. Mannheim Multihalle, the world's first bending-active grid shell for the German Architecture Exhibition, was built by Frei Otto, with the span and height of approximately 60 and 20 m, respectively [3]. Limited by computing technology at the time, the form-finding process was based on the hanging-chain method. Hence, some deviation exists in the obtained grid shell

<sup>\*</sup> Corresponding author.

E-mail address: [fengpeng@tsinghua.edu.cn](mailto:fengpeng@tsinghua.edu.cn) (P. Feng).

<https://doi.org/10.1016/j.engstruct.2024.118565>

Received 10 March 2024; Received in revised form 2 June 2024; Accepted 2 July 2024

Available online 16 July 2024

0141-0296/© 2024 Elsevier Ltd. All rights reserved, including those for text and data mining, AI training, and similar technologies.

morphologies [4]. Such construction process can be roughly divided into two steps: 1) scaffolding towers lifted by forklift trucks are used to push the plain mesh into its three-dimensional shape; 2) bolts are tightened so that rods at the connections cannot be misaligned, and the boundaries are fixed once the final shape is achieved [5]. Buro Happold also utilized the aforementioned bending-active concept to construct various buildings, such as Earth Centre, Japan Pavilion, Downland Museum, and Savill Garden [6–10]. S. Puystiens et al. came up with a new type of large-span membrane structure comprised of a bending-active ring and beam elements, contraction cables, and membranes [11]. By changing the amount of prestress in cables and membranes, the initially flat structure can transform into a three-dimensional pringle-shape [12]. E. Kriklenko et al. achieved the bending-active membrane structure by threading, and used a particle spring system for form-finding [13]. The SOFISTiK team presented a simple technique ACTB for creating bending-active beams and found it difficult to introduce a significant torsional bending in bending-active structures [14]. Daniel Sonntag et al. introduced a kind of double-curved shell structures, whose segmented flat timber shells were bent into the designed shapes and connected by a traditional textile connection method, achieving large span with less material use [15]. Moreover, the ICD/ITKE Research Pavilion, constructed at University of Stuttgart in 2010, reflects the idea of bending-active concept by changing the width and interaction of plywood panels [16].

In terms of materials, if bending-active concept is applied to create a shape, components generally incur significant internal stresses, which accordingly imposes certain requirements on the material's mechanical properties. Kotelnikova-Weiler et al. proposed the evaluation indicators for bending-active material properties, including elastic limit strain, stiffness, tenacity, price, environmental properties, and high durability [17]. According to their analysis, fiber-reinforced polymer (FRP), an emerging high-performance material comprised of fiber reinforcement and resin matrix, is very suitable for bending-active construction. Among various types of FRPs, CFRP has many advantages, including high chemical stability, excellent mechanical properties, and strong designability [18,19]. It is worth noting that the ultimate rupture strain of pultruded CFRP rods is around 1.5 %, while 2.5 % for glass FRP (GFRP) and 3 % for aramid FRP (AFRP) [20,21].

Tayeb, F et al. constructed a temporary lattice spatial structure called the Soliday Pavilion by using 12 m GFRP rods, which were first assembled on the ground and then lifted to their designated positions by construction struts, with their ends anchored to the foundations [22,23]. Similarly, Nicholas, P et al. used GFRP rods for the construction of the Faraday Pavilion at Roskilde Festival 2012 and conducted three-point bending tests and nonlinear finite element analysis (FEA) of the whole structure [24]. Moreover, W.X. Huang et al. constructed a double-layer GFRP grid shell, Mobius Pavilion, encompassed over an area of  $10 \times 10$  m with its highest point of 4 m [25].

Although the bending-active concept has been applied in many engineering cases, some key issues still need to be addressed. On one hand, it is difficult to bend a large cross-sectional FRP component into a large curvature, and its internal stress after forming is also quite high, which is not conducive to subsequent loading. Besides, its transportation cost may be very high. On the other hand, the stiffness of the component needs to be adjusted along the axis to achieve form-finding, that is, a variable cross-section is needed. A tricky problem is that a single component typically cannot achieve variable cross-section along the axis mainly because it is difficult for the pultrusion process to produce variable cross-section FRP components.

Therefore, this paper introduces a novel construction method for bunched rods, which enables the self-shaping construction of complex curved free-form spatial structures. This method offers several

advantages, including strong designability, short construction period, graceful appearance, and ease of implementing large-scale structures.

To develop the abovementioned structural system, the paper undertakes the following key tasks:

- A novel method implementing the bending-active concept is proposed by using straight components with variable cross-section (or bending stiffness) to alter the curvature. This enables the component to form certain curved shapes under given loads automatically.
- Specific methods for form-finding and inverse processes of the bunched rods are proposed based on the large deformation theory. These methods are further verified through FEA and experimental investigations.
- A practical design case study of a saddle-shaped canopy demonstrates the feasibility of the proposed design method and self-shaping system in complex curved surface construction. The findings of this study can guide actual engineering projects.

## 2. Concept of bending-active bunched CFRP rods

### 2.1. Construction of bunched CFRP rods

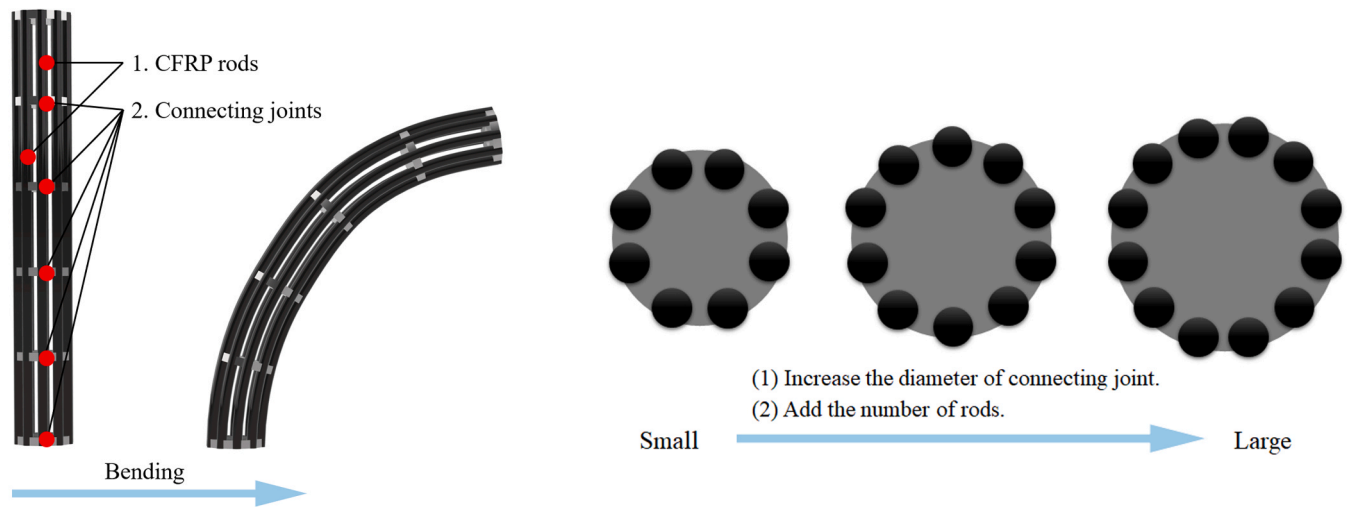
Based on the bending-active concept, the design method for a free-form spatial structure system with complex curved shapes can be achieved by variable cross-section bunched CFRP rods.

Fig. 1(a) shows the construction of bunched CFRP rods, where 1 and 2 represent single CFRP rod and connecting joint respectively. The connecting joint has multiple positioning holes, through which slender CFRP rods with smaller diameters and lower rigidity can pass one-to-one. In this way, CFRP rods can be relatively fixed in position with connecting joints by friction and adhesion forces, then a component with a much larger cross-sectional area can be formed, which allows multiple slender rods to work together and saves material use compared to the big cross-section rod with the same stiffness. The variable cross-sections of the bunched CFRP rods are achieved by changing the size of the connecting joints and the number of slender CFRP rods, as shown in Fig. 1 (b). When the cross-sectional area of a component needs to be increased, connecting joints with larger diameters can be used, and rods can be added as required. On the contrary, when the cross-sectional area needs to be reduced, connecting joints with smaller diameters can be used, and redundant rods should be cut off at the next joint.

The terms “rod” and “component” are further elaborated here to avoid confusion. In this paper, a “rod” refers to a single member, while a “component” is made up of rods, including bunched CFRP rods mentioned here and bending test components mentioned in Section 4. To sum up, as shown in Fig. 2, the structure is composed of components, and components are composed of rods.

In the application of bending-active concept, the bunched CFRP rods proposed above can effectively solve these two key problems mentioned in Section 1.

- A construction method called “separation-to-integration” is proposed to solve the problem of bending difficulty of a large cross-sectional CFRP rod into a large curvature. That is, before assembly, those straight rods are pre-bent separately to have a certain initial curvature and then sequentially threaded through the positioning holes of connecting joints to form an entire component. Of course, the CFRP rods and connecting joints can be transported separately in the actual construction process, which can reduce the transportation cost.
- The fabrication of a single CFRP rod with variable cross-section directly by pultrusion is extremely hard, and additional processing such as CNC cutting is generally required. However, for the bunched



(a) Straight and deformed bunched CFRP rods.

(b) Cross sections of bunched CFRP rods with different dimensions.

Fig. 1. The schematic diagram of bunched CFRP rods' construction.

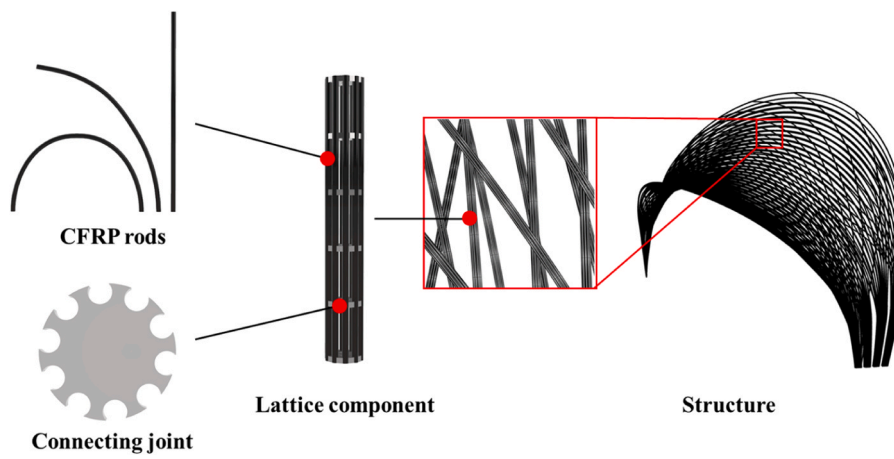


Fig. 2. The interrelationship of rod, component and structure.

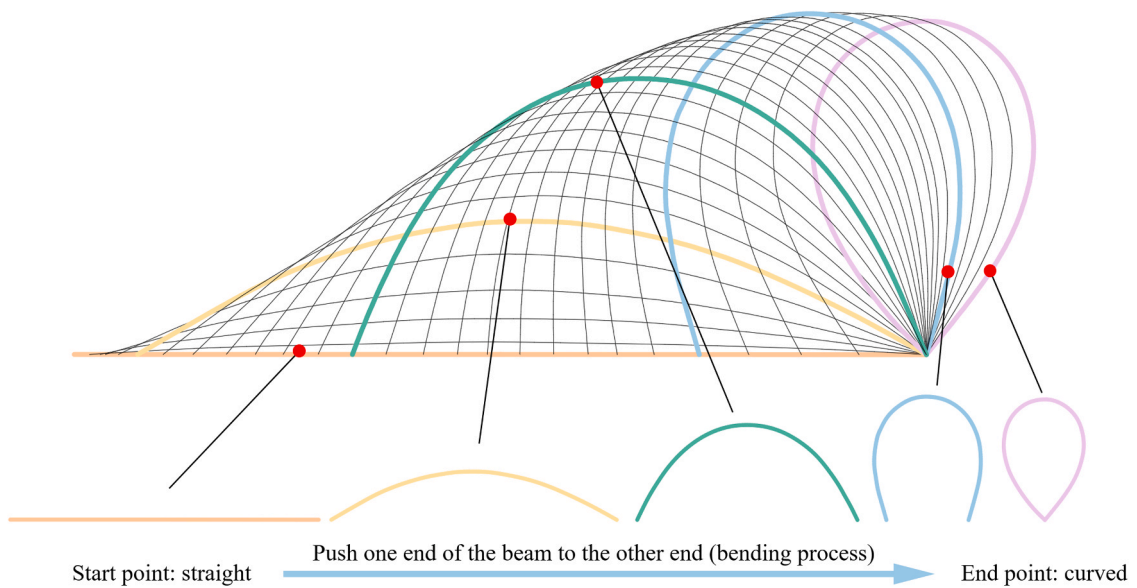


Fig. 3. A single span beam from straight to the configuration with the maximum deformation.

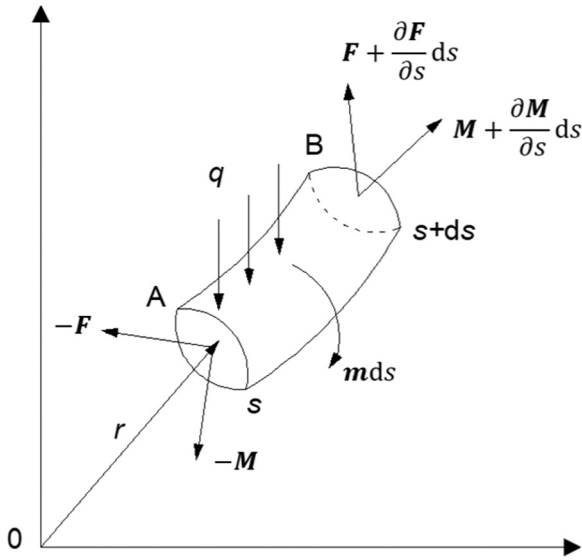


Fig. 4. Force analysis of the micro-segment AB.

CFRP rods, variable cross-section can be fulfilled by changing the size of the connecting joints and the number of slender CFRP rods mentioned above. Hence, large deformation components with complex forms can be further realized.

### 2.2. Basic mechanical behavior of elastic component

The Bernoulli-Euler (BE) model and the Timoshenko model are the most common mathematical models for beams in structural mechanics. Because the slenderness ratio of bunched CFRP rods is usually very large, it can be regarded as BE component in mechanical analysis. Levien summarized in detail the process by which scientists of all generations calculated the geometry of elastic bent beams [26]. One of the landmark events is that Euler published the first completely characterized family of Elastica curves based on variational techniques in 1744, as shown in Fig. 3 [27]. Nowadays, the problem of the Elastica can be approached from many different angles, including the calculus of variations, elliptical integrals and mechanical equilibrium.

The first approach involves complex mathematical methods to develop closed form solutions. As known to all, Elastica is a curve that generates a minimum of potential bending energy in a constrained system. Besides, potential energy of a bent component behaves proportionately to the square of the local curvature, as shown in Eq. (1), where  $1/\rho(x)$  is the curvature at different  $x$  coordinates,  $\tilde{E}$  is total bending energy, and  $l$  is the length of the deformed component. The solution to this minimum energy problem involves calculus of variations which is not followed up here, since the limited and purely geometric description of the Elastica is not practical for the design of bending-active structures.

The Bernoulli-Euler law formulates a second order nonlinear differential equation for large nonlinear deformations, as shown in Eq. (2) [28], where  $w(x)$  and  $M(x)$  are the deflection and bending moment at different  $x$  coordinates, and  $EI$  is the bending stiffness of the component. The elliptical integral method is to solve Eq. (2) by integration. It can only solve some typical buckling deformation problems, that is, it is also not applicable to the components under complex boundary & load conditions.

$$\tilde{E}[1/\rho(x)] = \frac{1}{2} \int_0^l EI[1/\rho(x)]^2 dx \quad (1)$$

$$\frac{1}{\rho(x)} = \frac{w''(x)}{[1 + w'(x)^2]^{2/3}} = -\frac{M(x)}{EI} \quad (2)$$

Hence, mechanical equilibrium method is adopted in this paper to solve the deformation problem of components under complex conditions, mainly introduced in Section 3.1.

## 3. Analysis of structural form-finding and inverse processes

### 3.1. Structural form-finding process: large deformation theory and FEA

Calculating the deformation of components under the given stiffness and boundary & load conditions is defined as structural form-finding process. The above process can be achieved through FEA or theoretical calculation, and the FEA results can be used as the verification of the large deformation theoretical analysis results.

In the large deformation theory, an object can be referred to as a rod if its lateral dimension is much smaller than its length. The following assumptions are made for large deformation rods: 1) the interaction forces among the rods are known and considered as concentrated forces acting at a point on the rod, that is, only considering the relationship between rod deformation and applied external forces; 2) Kirchhoff's assumption is used in deriving the deformation equations of the rod, which assumes that the cross-sections perpendicular to the axis of the rod remain plane after deformation and are still perpendicular to the deformed central axis.

A micro-segment AB of the deformed rod is taken out to analyze its instantaneous stress state, as shown in Fig. 4, where  $s$  is the one-dimensional drag coordinate along the central axis of the rod;  $r$  is the position vector of the micro-segment centroid relative to fixed point O;  $F$  and  $M$  are the force and moment vectors acting on the section A or B;  $\gamma$  is mass per unit length;  $q$  is the external force vector acting on the micro-segment and  $m$  is the body moment or surface moment per unit length. Hence, the angular momentum  $L$  of the micro-segment can be derived from Eq. (3), where “ $\times$ ” represents the vector product. Eq. (4) can be obtained from the momentum theorem and Eq. (5) is from the momentum theorem. Eq. (6) can be further obtained by Eq. (4) and Eq. (5) [29].

$$L = r \times q = \gamma(s) \left( r \times \frac{\partial r}{\partial t} \right) ds \quad (3)$$

$$\frac{\partial}{\partial t} \left[ \gamma(s) \frac{\partial r}{\partial t} \right] = \frac{\partial F}{\partial s} + q \quad (4)$$

$$\gamma \left( r \times \frac{\partial^2 r}{\partial t^2} \right) = \frac{\partial}{\partial s} (r \times F) + \left( F + \frac{\partial F}{\partial s} ds \right) + \frac{\partial M}{\partial s} + m + r \times q \quad (5)$$

$$\frac{\partial r}{\partial s} \times F + \frac{\partial M}{\partial s} + m = 0 \quad (6)$$

Decomposing the vectors in Eq. (6) along the natural coordinates ( $g_1, g_2, g_3$ ) yields the expression of the motion equation along the natural coordinates, i.e., Eq. (7), where  $g_1$  is directed along the tangent direction of the rod and pointing to the side where  $s$  increases;  $1/\rho$  and  $1/\tau$  are the curvature and torsion, respectively;  $g_1$  is the length transformation coefficient, which can be calculated by Eq. (8); the length of the micro segment after deformation is  $ds$ ;  $a_1, a_2$  and  $a_3$  are the acceleration components in three directions.

If the rod moves in the plane, i.e., the XY plane coordinate system, then  $1/\tau = 0, F_3 = q_3 = 0, M_1 = M_2 = m_1 = m_2 = 0$ . Therefore, Eq. (7) can be simplified to Eq. (9), which is the motion equation of the rod in the plane. In the large deformation analysis of the rod in this paper, the acceleration is zero because the static equilibrium state is considered.

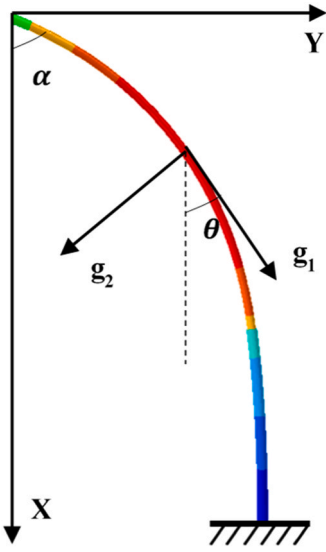


Fig. 5. X and Y coordinate direction identification.

$$\begin{cases} \gamma a_1 = \frac{1}{g_1} \frac{\partial(F_1 g_1)}{\partial s} - F_2 \frac{1}{\rho} + q_1 & (a) \\ \gamma a_2 = \frac{\partial F_2}{\partial s} + F_1 \frac{g_1^2}{\rho} - F_3 \frac{g_1}{\tau} + q_2 & (b) \\ \gamma a_3 = \frac{\partial F_3}{\partial s} + F_2 \frac{g_1}{\tau} + q_3 & (c) \\ 0 = \frac{1}{g_1} \frac{\partial(M_1 g_1)}{\partial s} - M_2 \frac{1}{\rho} + m_1 & (d) \\ 0 = \frac{\partial M_2}{\partial s} + M_1 \frac{g_1^2}{\rho} - M_3 \frac{g_1}{\tau} - g_1 F_3 + m_2 & (e) \\ 0 = \frac{\partial M_3}{\partial s} + M_2 \frac{g_1}{\tau} + g_1 F_2 + m_3 & (f) \end{cases} \quad (7)$$

$$g_1 = \left| \frac{\partial \mathbf{r}}{\partial s} \right| = \frac{ds}{ds} \quad (8)$$

$$\begin{cases} \gamma a_1 = \frac{1}{g_1} \frac{\partial(F_1 g_1)}{\partial s} - F_2 \frac{1}{\rho} + q_1 & (a) \\ \gamma a_2 = \frac{\partial F_2}{\partial s} - F_1 \frac{g_1^2}{\rho} + q_2 & (b) \\ 0 = \frac{\partial M_3}{\partial s} + g_1 F_2 + m_3 & (c) \end{cases} \quad (9)$$

It is assumed that the angle between the tangent direction at the end of the rod and the vertical direction is  $\theta$  ( $\theta = \alpha$  at the left and  $\theta = 0$  at the right), as shown in Fig. 5. By bringing the known conditions into the motion equation of the rod, Eq. (9a) and (9b) are automatically satisfied when the rod is statically balanced, and Eq. (9c) can be written in the

$$\begin{cases} x = \int_0^s \cos\theta ds = \int_{\theta=\frac{\pi}{2}}^{\theta=0} \frac{\cos\theta}{\sqrt{\frac{2}{E(\theta)I(\theta)} [F_2(\cos\theta - \cos\alpha) + F_1(\sin\theta - \sin\alpha)] + \left(\frac{M_3}{E(\theta)I(\theta)}\right)^2}} d\theta \\ y = \int_0^s \sin\theta ds = \int_{\theta=\frac{\pi}{2}}^{\theta=0} \frac{\sin\theta}{\sqrt{\frac{2}{E(\theta)I(\theta)} [F_2(\cos\theta - \cos\alpha) + F_1(\sin\theta - \sin\alpha)] + \left(\frac{M_3}{E(\theta)I(\theta)}\right)^2}} d\theta \end{cases} \quad (13)$$

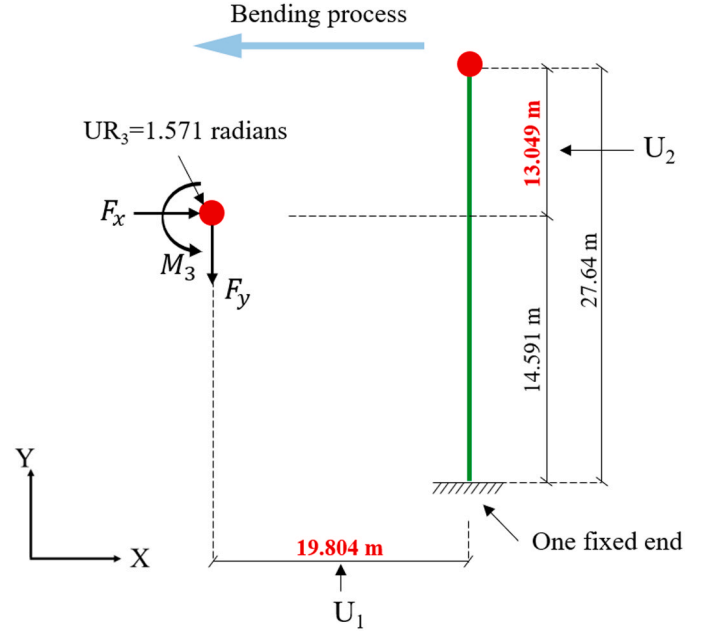


Fig. 6. Boundary & load conditions of a half rod ( $F_x$ ,  $F_y$ ,  $M_3$  in Table 1, displacement and rotation  $U_1$ ,  $U_2$ ,  $UR_3$  in FEA are shown).

form of Eq. (10). Multiplying both sides of the equation by  $d\theta/ds$  and integrating yields Eq. (11), where the bending moment is  $M_3$  at the left endpoint, hence the curvature is  $M_3/EI$ . Simplifying this expression yields the relationship between  $\theta$  and  $s$ , as shown in Eq. (12).

$$EI \frac{d^2\theta}{ds^2} = -(F_2 \sin\theta - F_1 \cos\theta) \quad (10)$$

$$\frac{EI}{2} \int_{\theta=\alpha}^{\theta} d\left(\frac{d\theta}{ds}\right)^2 = F_2 \int_{\theta=\alpha}^{\theta} \frac{d\cos\theta}{ds} + F_1 \int_{\theta=\alpha}^{\theta} \frac{d\sin\theta}{ds} \quad (11)$$

$$\frac{EI}{2} \left[ \left(\frac{d\theta}{ds}\right)^2 - \left(\frac{M_3}{EI}\right)^2 \right] = F_2(\cos\theta - \cos\alpha) + F_1(\sin\theta - \sin\alpha) \quad (12)$$

$$\frac{d\theta}{ds} = -\sqrt{\frac{2}{EI} [F_2(\cos\theta - \cos\alpha) + F_1(\sin\theta - \sin\alpha)] + \left(\frac{M_3}{EI}\right)^2} \quad (12)$$

The X and Y coordinate directions are shown in Fig. 5. Hence, the displacement of the X and Y directions at the left endpoint can be obtained by integrating along the rod, as shown in Eq. (13). It should be noticed that the stiffness  $EI$  is changed into  $E(\theta)I(\theta)$  in Eq. (13). During the self-shaping design process in this paper,  $I$  changes with the independent variable  $s$  or  $\theta$  but  $E$  remains constant because of the unchanged material. However, to account for the universality of the formula and incorporate advancements in technologies (such as 3D printing using various materials),  $E$  has the potential to be altered. Therefore, the notation  $E(\theta)$  is employed in Eq. (13).

A finite element model of slender rod was established to verify the reliability and validity of the above theory. Assuming the rod's cross-section was circular, with both ends fixed on a horizontal plane. The ends' axial direction was perpendicular to the plane, and the length of the rod  $L$  was 27.64 m (taking the length of the most marginal component in the design case in Section 5). Only half of the rod needed to be analyzed in FEA due to symmetry, as shown in Fig. 6. The commercial finite element software ABAQUS was chosen to analyze the deformation and stress of objects (including rods, components or the total structure) in this paper. In the Property module, the section of the rod was arranged in beam type. In the Step module, the Nlgeom option should be turned on for large deformation calculation. One end of the rod was fixed, meaning that all the displacements and angles were restricted, and the other end was under a given rotation and displacement (namely,  $U_1 = -19.804$  m,  $U_2 = -13.049$  m,  $UR_3 = 1.571$  radians). Because the rod's slenderness ratio is too large, applying both rotation and displacement at the same time will lead to distortion near the end of the rod, making it difficult to bend into the target shape, as shown in Fig. 7. Therefore, in the Step module, three static steps were set to successively apply  $U_1$ ,  $UR_3$  and  $U_2$  on one end of the rod. After meshing the rod, the type of each element was B32 (a 3-node quadratic beam in space), and the mesh sizes (representing the size of element) were set to 100 mm, 50 mm, and 25 mm.

The calculation results of rod-end reaction forces are presented in Table 1 (the numbers in parentheses are relative error compared to mesh size 100 mm). The mesh convergence analysis aims to investigate the degree of sensitivity of computational results to mesh size variation. In order to determine the accuracy, the FEM results ( $F_x$ ,  $F_y$ , and  $M_3$  in Fig. 6) for different mesh sizes (50 mm and 25 mm) were compared to those obtained from 100 mm. If the discrepancies were minimal, it indicated that the 100 mm mesh size was capable to generate relatively precise FEA results. Table 1 shows that, when the mesh size was reduced to half (50 mm), the discrepancies in  $F_x$  and  $M_3$  were 3.10 % and 0.33 %, respectively. Further reducing to a quarter (25 mm), the discrepancies in  $F_x$  and  $M_3$  were 9.39 % and 0.31 % respectively. Since  $F_x$  had a magnitude two orders higher than  $F_y$ , the left end of rod could be regarded as a sliding support condition, and therefore, the  $F_y$  result was not considered in this analysis. Conclusively, considering both accuracy and computational efficiency, a 100 mm mesh size proves to be sufficiently fine for numerical analysis.

Subsequently, the theoretical results of left endpoint's displacement (18.011 m and 14.620 m respectively) was computed with the input of reaction forces from FEA analysis using 100 mm mesh size. The theoretical results were compared with the FEA input ( $|U_1| = 19.804$  m,  $|L-U_2| = 14.591$  m), and the relative error was within 1 %, which validated the effectiveness of the large deformation theory. Two points are worth noting here. On one hand, the theoretical solutions should have considered the elongation of the rod (i.e.,  $g_1 \neq 1$ ). On the other hand, the

**Table 1**  
Mesh convergence analysis results in FEA.

Mesh size (mm)		100	50	25
Reaction forces of rod's end	$F_x$ (N)	116.363	119.972 (3.10 %)	127.290 (9.39 %)
	$F_y$ (N)	-8.506	-8.971 (5.47 %)	-1.732 (79.6 %)
	$M_3$ (N-mm)	3986.290	3973.130 (0.33 %)	3973.990 (0.31 %)

rod may exist with an inflection point under external forces and moments as shown in Fig. 7. In such case, the calculation of displacement in X and Y directions requires integration in two segments from 0 to  $\beta$  and from  $\beta$  to  $\pi/2$  based on Eq. (13).

In a word, through large deformation theory and FEA, it is mighty feasible to calculate the rod's deformation under the given stiffness, boundary, and load conditions.

### 3.2. Inverse form-finding method: segmented calculation method

The inverse form-finding calculation method is used to determine the stiffness distribution along the axis of a component based on its deformed shape and external load conditions. Using the idea of calculus, the segmented calculation method is proposed. It first divides a certain length of the component into several small sections, and then calculates the bending stiffness of each section based on its own deformation. Two approaches can be employed to achieve this: database and theoretical solution.

The first approach comprises two main steps: 1) establish a database of components' deformation modes under different variable cross-sections with the same boundary & load conditions; 2) select the corresponding variable cross-section form by comparing the given shape with those in the database. The process of building the database is illustrated on the left side of Fig. 8. To begin with, a straight component with the same length as the given one is created in the finite element software. After that, the component is divided into several sections and assigned a cross-sectional property  $A_i$ . And then, the boundary & load conditions are applied to calculate the shape, and the coordinates of nodes on the component  $B_i$  are derived. At last, a database including  $B_1, B_2, \dots, B_n$  can be obtained after  $n$  iterations. The process of determining the component's variable cross-section form is illustrated on the right side of Fig. 8. First, the target component is divided into equal sections and the coordinates are exported. Then, calculate the discrepancy between the above and those in the database. Hence, the least discrepant component's variable cross-section form will be finally determined. This approach is selected in this paper.

Another approach which can obtain the cross-section forms is the theoretical solution. When the component's deformation is known, the bending stiffness  $EI$  of each small section can be obtained by directly solving Eq. (13), that is, the cross-section of each segment is obtained. Further, the variable cross-section form of the entire component can be obtained by extracting the deformation data of each section and calculating their bending stiffness in turn.

Particularly worth mentioning here is that the above calculation obtained is the bending stiffness  $EI$  distribution of the component along its axis. To establish the relation between  $EI$  and the section shape of the component, it can be achieved in the following two ways:

- If connecting joints of the bunched CFRP rods are dense enough, Kirchhoff's assumption can be assumed tenable. Thus, the theoretical  $EI$  of the section can be calculated directly and compared with results of segmented calculation method. When the two are consistent (or close), the relation between component section and  $EI$  can be established.

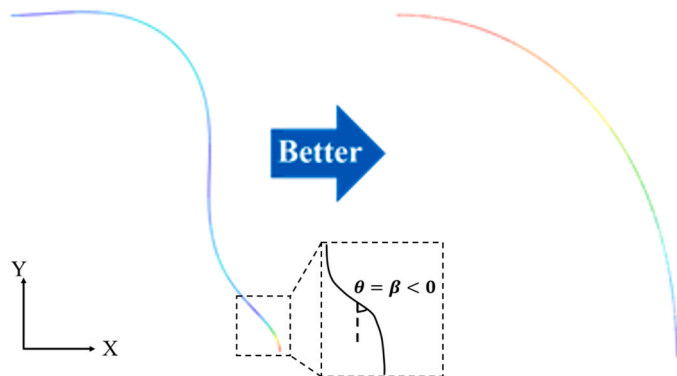


**Fig. 7.** The FEA results (right figure shows the ideal calculation result, and the inflection point is defined).

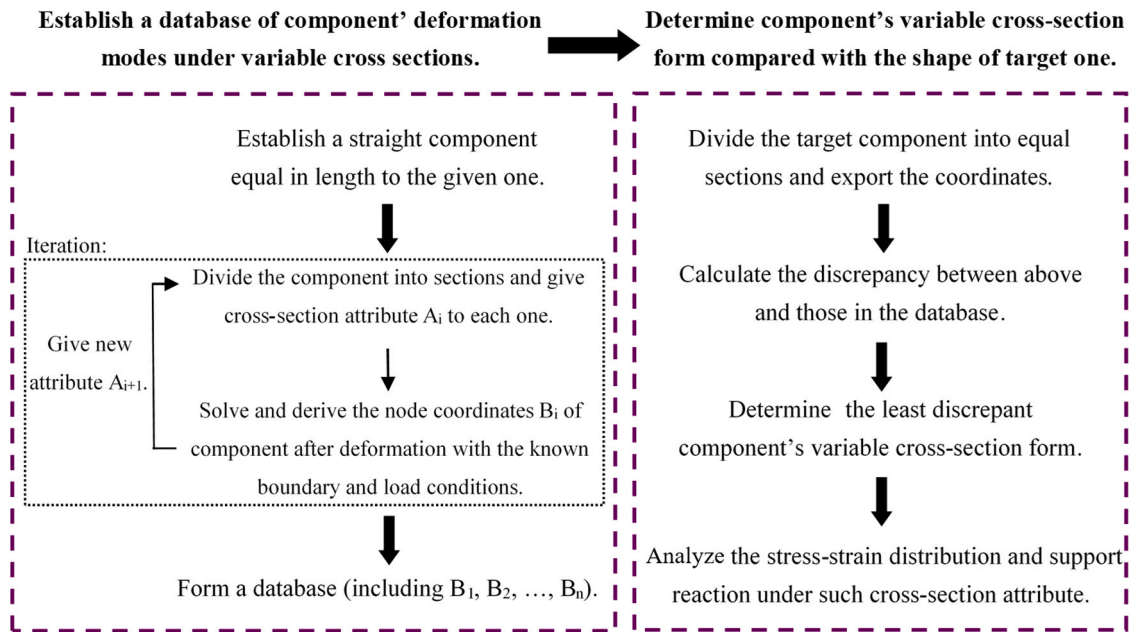


Fig. 8. The flowchart of segmented calculation method.

- If the distance between connecting joints is too large to meet Kirchhoff's assumption, it is necessary to establish a finite element model of the component, and apply a unit angle at both ends to get the bending moment. The equivalent EI is equal to  $M\rho$ , where  $\rho$  is the curvature radius of the bending component.

#### 4. Experimental investigation on bending properties of CFRP components

##### 4.1. Scheme and process

To further verify the structural form-finding results from the large deformation theory and FEA, the planar bending tests have been designed for slender components.

All components in the experiment were made of CFRP, whose resin and fiber content were about 26 % and 74 %, respectively. Based on the test results of material properties, the average tensile strength of a CFRP rod with a diameter of 8 mm was 2416 MPa, and its tensile elastic modulus was 163.5 GPa. Those components were 9 m long and divided into two types: single rod (SR) and variable-section component (VC), as shown in Fig. 9. Here, the cross-section of SR was circular with a diameter of 7.3 mm, while VC was composed of one 9 m main rod and four 3 m auxiliary rods. In the bending tests, auxiliary rods were attached to both ends of the main rod with tape to ensure that they could work together. There is no obvious slipping between them during the tests. However, in real-world applications, the number of rods contained

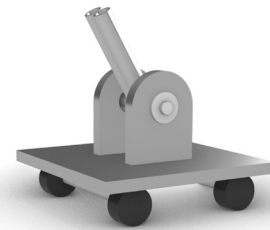


Fig. 10. The schematic diagram of sliding steel base.

in a component is much greater than the above. In such cases, specially designed joints are indispensable for effectively connecting and forming the overall spatial structure. Besides, due to low bending stiffness of SR, it is prone to out-of-plane instability. Therefore, the 3D printed connector was designed to connect two SRs horizontally together (with internals of 1 m) to improve their out-of-plane stiffness.

The two ends of tested components were connected to two sliding steel bases, one of which was fixed, and the other was pushed to bend the component (the moving path is shown by the yellow arrow in Fig. 11). The support condition could be change between fixed with certain angles and pinned by adjusting the fastening force of the bolt shown in Fig. 10. The angle between component axis and the ground is mentioned in Table 2, where “45 or 90°” and “-” means the connection is fixed or

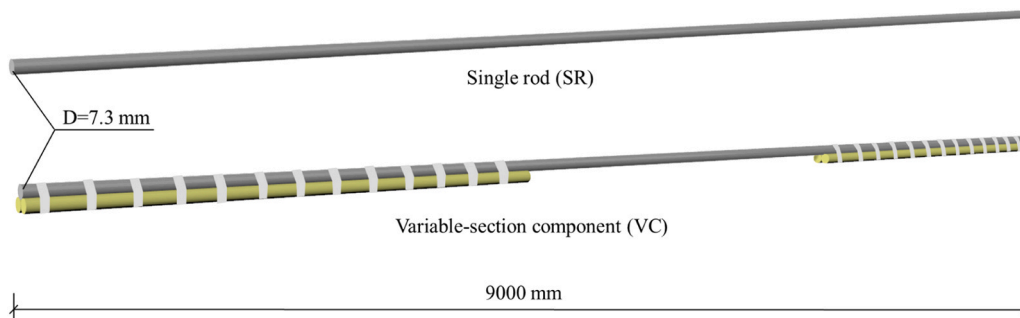


Fig. 9. The experiment components (SR and VC).

**Table 2**  
Bending test setup of nine specimens.

Specimen	Testing number	Span (mm)	Support angle (°)	Load conditions
Single component (SR)	SR-0	5720	-	-
	SR-1	7352	45	Self-weight
	SR-2	5720	-	Self-weight
	SR-3	5720	90	Self-weight
	SR-4	5720	90	Self-weight + concentrated load
Variable-section component (VC)	VC-1	7352	45	Self-weight
	VC-2	5720	-	Self-weight
	VC-3	5720	90	Self-weight
	VC-4	5720	90	Self-weight + concentrated load

pinned, respectively. In the “SR-0” case, the rod was laying horizontally on the ground to avoid the influence of self-weight.

The shape of the component was measured by a total station and its vertical displacement at midspan was measured by a displacement gauge. The SR and VC components were both measured at four loading stages as follows:

- Stage 1: The two ends of the component were 7352 mm apart, both fixed with an angle of 45° between the axis of the component to the ground (SR-1 and VC-1).
- Stage 2: The two ends of the component were 5720 mm apart, and the rotation at both ends of the component were not restricted, namely pinned (SR-2 and VC-2).
- Stage 3: The two ends of the component were 5720 mm apart, both fixed with an angle of 90° between the axis of the component to the ground (SR-3 and VC-3).
- Stage 4: Based on Stage 3, three 2 kg weights were added and separately hung at three points as shown in Fig. 11 (SR-4 and VC-4). During the process of hanging weights, the out-of-plane displacement was limited by pulling a horizontal thin string at midspan.

Therefore, there are nine different working conditions in total, as shown in Table 2. It is worth noting that SR-0 to SR-4 are five different working conditions (due to changes in boundary conditions and external loads) of the same component SR, which also applies to VC.

#### 4.2. Deformation analysis

FEA outlined in Section 3.1 was used to simulate the deformation shape of the components under different working conditions. Comparing the FEA results with bending test results, as shown in Table 4. The red curve represents the test result and the yellow dotted curve represents the FEA result. The calculation result of  $R^2$  (coefficient of determination) approaches 1, indicating better agreement between the deformation shape obtained from the test and FEA. Errors primarily originate from the self-weight of the wires connected to the displacement gauge, which slightly increases the deformation of the components.

The displacement in the X and Y directions in the span of the

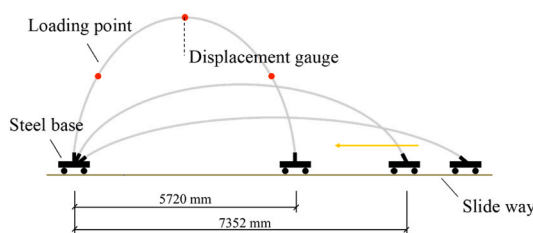


Fig. 11. The process of the bending test.

**Table 3**  
Results of Y coordinates comparison in span of the rod.

Testing number	Experiment (mm)	FEA (mm)	Large deformation theory (mm)
SR-0	3029	3040 (0.36 %)	2982 (1.55 %)
SR-1	2237	2344 (4.78 %)	2409 (7.69 %)
SR-2	3034	3031 (0.10 %)	3225 (6.29 %)
SR-3	2891	2856 (1.21 %)	3036 (5.02 %)
SR-4	2281	2200 (3.55 %)	2133 (6.49 %)
VC-1	2479	2460 (0.77 %)	2606 (5.12 %)
VC-2	3201	3316 (3.59 %)	3373 (5.37 %)
VC-3	2993	3007 (0.47 %)	3094 (3.37 %)
VC-4	2824	2885 (2.16 %)	2949 (4.43 %)

component could be obtained by the large deformation theory in Section 3.1, and the results are shown as blue crosses in Table 4. The midspan Y coordinates calculated by FEA and theory were compared with experimental results, as shown in Table 3 (the numbers in parentheses are relative error compared to experimental results).

Since the self-weight of components was not considered in the calculation process, the results of displacement in Y direction were generally larger than the experimental and FEA results. However, the comparison of SR-0 and SR-2 shows that the impact of self-weight on the deformation of the component is small enough to be ignored. By comparing the deformation of components in SR group and VC group under the same boundary & load conditions, the fact is discovered that shapes of SR components are fuller while the two ends of VC ones show less curvature due to greater stiffness. Note that the specimen SR-4 has an inflection point. Hence, it is necessary to extract the coordinates of this inflection point and integral into two sections, as mentioned in Section 3.1.

The above results demonstrate that FEA can accurately calculate the deformation of SR and VC under different boundary & external load conditions, and the theoretical calculation method can obtain the vertical displacement at midspan. Realization of form-finding process provides a solid foundation for subsequent reverse process.

## 5. Design case

### 5.1. Saddle-shaped curved spatial structure design process

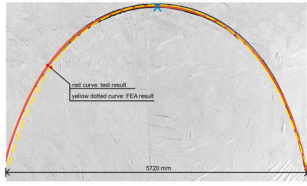
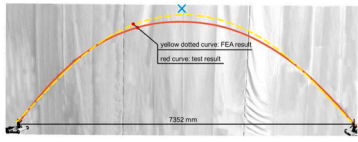
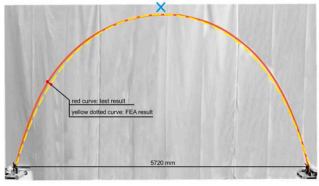
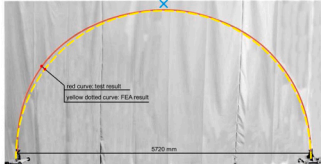
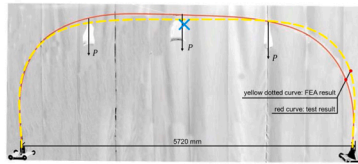
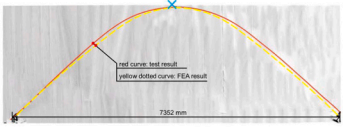
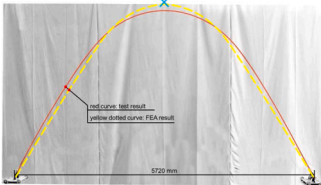
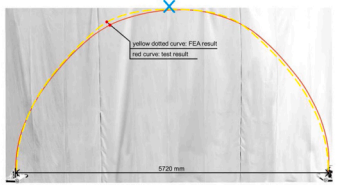
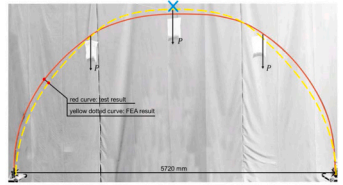
#### 5.1.1. Geometric discretization method

The design process of free-form spatial structures proposed in this paper has two main steps: 1) transform the complex surfaces into a braided mesh curve system, that is, discretizing the given surfaces into a certain number of curves; 2) determine the variable cross-section form for each rod to enable it to automatically deform into the shape of the corresponding curve under given boundary conditions.

The most fundamental work is discretizing the surface into a curve system if one wishes to construct a spatial structure using CFRP rods. To describe the density of the curve system, the filling rate  $\varphi$  is introduced to quantify it as shown in Eq. (14), where  $S$  represents the surface area;  $n$  represents the total number of curves;  $t$  represents the hypothetical curve width and  $l_i$  represents the length of the  $i$ th curve. When the filling rate exceeds 30–35 %, the curve system is considered dense and tight.

$$\varphi = \frac{\sum_{i=1}^n t \cdot l_i}{S} \times 100\% \quad (14)$$

**Table 4**  
Comparison of deformed shapes from bending tests and FEA results.

Testing number	SR-0	SR-1	SR-2
Component deformation			
R <sup>2</sup>	0.995	0.988	0.997
Testing number	SR-3	SR-4	VC-1
Component deformation			
R <sup>2</sup>	0.998	0.960	0.987
Testing number	VC-2	VC-3	VC-4
Component deformation			
R <sup>2</sup>	0.989	0.999	0.991

The red curve represents the test result; the yellow dotted curve represents the FEA result; the blue cross represents the result of large deformation theory.

There are two ways to discretize surfaces: 1) sample multiple points on the surface according to certain attributes, then connect them into curves by surface fitting algorithms (such as least-square algorithm); 2) parameterize the surface to a plane, where straight lines or curves are laid on, then map those lines and curves onto the original surface. The computational amount of the first way is lower, but the precision is less since only a limited number of points on the surface are used to fix a curve. In addition, since the connection of points into lines (or curves) has no additional constraints, the generated curves may be irregular. Whereas, the second way can accurately project the target curve onto the original surface based on the surface boundary while considering the filling rate. Noted that the surface needs to be subdivided into grids before parameterization, and Dirichlet energy minimization [30] or convex combinations [31] can be chosen for two-dimensional parameterization. Here, Luo et al. have implemented boundary-conformed tool path generation based on global reparameterization using the above

methods [32].

The second step of the design process, namely determining the form of each component has been discussed in Section 3.2.

### 5.1.2. Structure design and details

A saddle-shaped curved spatial structure is designed based on the construction of self-shaping CFRP structural system and segmented calculation method discussed in Section 3.2. The appearance of the structure is shown in Fig. 12. The structure has a span of 33.8 m, a maximum height of 22.3 m, and is composed of 107 structural components. Here, 80 of them are arranged along the span direction (L0 and L1 layers) with the full length, while the other 27 penetrating components (L2 layer) integrate into a three-dimensional woven network. L0, L2, and L1 layers are stacked on top of each other in order from top to bottom. The filling rate  $\varphi$  is 45.11 % (where  $t = 62$  mm,  $S = 761.11$  m<sup>2</sup>), which means such curve system is dense enough.

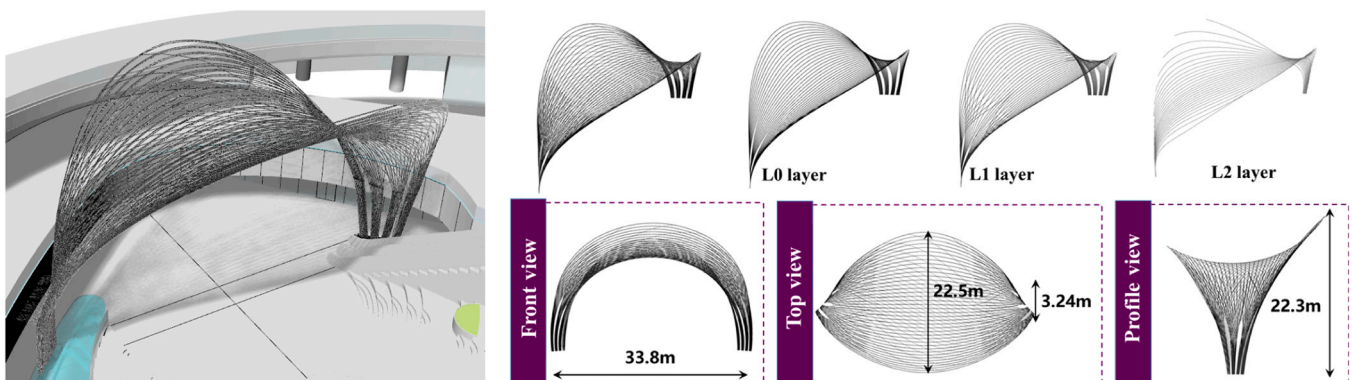


**Fig. 12.** The saddle-shaped curved spatial structure.

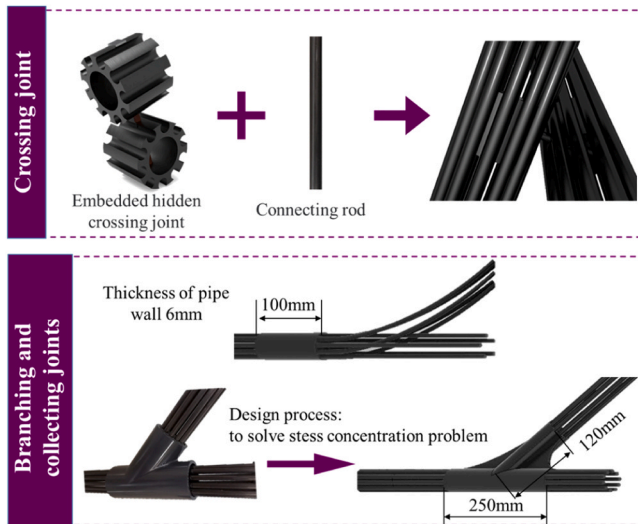


Fig. 13. Construction details of crossing joint, branching, and collecting joints.

The adjacent bunched CFRP rods are connected by two types of steel joints, as shown in Fig. 13, each with its specific advantages:

- (1) The first joint is called “embedded hidden crossing joint”, mainly composed of two sleeves and a connecting rod, which is used to connect different layers with minimum impact on the overall appearance of the structure. The joint is fixed by adhesive and using arc-shaped pads and nuts at both ends of the connecting rod to prevent components from slipping.
- (2) The second type is called “branching and collecting joints”, including a hollow cylinder and shaped tee sleeve. The hollow cylinder is used to realize the shunt and confluence of L1 layer components, and the tee sleeve is to connect components in the front and back edges and those of L2 layer. They can be on the edge of or inside the structure, which improve the synergistic performance of bunched CFRP rods. By designing and optimizing the latter one, the stress concentration problem can be solved.

Each structural component mentioned above comprises single CFRP rods with a diameter of 12.2 mm. During actual construction process, the single CFRP rod can be wound beforehand into a circle to facilitate transportation. The synergy of the components is ensured by the connecting joints described in Section 2.1. Variable cross-sections can be realized by changing the size of the connecting joints and the number of CFRP rods in the same cross-section, which can be obtained by establishing a database of the deformation modes of the components with different cross-sections and comparing them with the designed shape.

When using the segmented calculation method, it is necessary to establish the relationship between EI and the section shape of the component as mentioned in Section 3.2. The length of components in this structure are tens of meters, but the spacing of connecting joints is 300 mm (determined in Section 5.2.1). Hence, it can be considered that components conform to Kirchhoff’s assumption, and the theoretical EI of the section can be calculated directly.

## 5.2. Loading and analysis

### 5.2.1. Static load and buckling analysis

The main part of this structure is made of CFRP, only little steel is used in connecting joints and basis. Besides, the comparison of SR-0 and SR-2 shows that the impact of self-weight on the deformation of one single component is minimal in Section 4.2. The above experimental phenomenon shows that the influence of self-weight on the structure is very small. Considering that the main application scenario is the open-

air entertainment platform, the structure is mainly not affected by other static loads except its own weight.

During the bending process of components, they may fail due to CFRP material damage or local instability of rods among connecting joints. It is needed to avoid buckling failure of a single CFRP rod in the structure by theoretical analysis. The formula for calculating the Euler buckling capacity of a single rod is shown in Eq. (15), with a calculation length coefficient  $\mu$  of 2. The buckling capacity can be controlled by adjusting the distance  $L$  between connecting joints. Thus, it is possible to theoretically avoid local buckling of the component by adjusting the value of  $L$ . Ten CFRP rods were selected as a component section for stability analysis. The diameters of the connecting joint and the positioning hole were 48.8 mm and 12.2 mm respectively. FEA was conducted on the bunched CFRP rods with the maximum curvature in the above engineering case. The maximum compressive stress of the rod obtained through FEA was 171.7 MPa, as shown in Fig. 14, which is much lower than the compressive strength of CFRP rod. With a spacing of 300 mm between connecting joints, the buckling load of a single CFRP rod was 21.6 kN, calculated by Eq. (15), and its compressive stress was 185 MPa (slightly greater than 171.7 MPa). Thus, the spacing of 300 mm in this case can ensure that the single CFRP rods will not experience buckling under compression.

$$P_{cr} = \frac{\pi^2 EI}{(\mu L)^2} = \frac{\pi^2 EI}{4L^2} \tag{15}$$

### 5.2.2. Dynamic load analysis

It is necessary to extract the basic mechanical model of the structure with external boundary & load conditions before FEA. Crossing, branching and collecting joints are fixed with bolts and adhesive mentioned in Section 5.1.2, hence considered to be rigid. The CFRP components are inserted into the preset holes of the ground base, so they are fixed supports. As can be seen from Fig. 12, the structure is also in contact with the first floor. Since such contact does not limit the rotation of the components, it can be considered as hinged.

Snow load was not considered because the structure will be built in a low latitude area of China. Only the influence of wind load was evaluated. According to load code for the design of building structures (GB50009–2012), wind load can be calculated by Eq. (16), where  $w_0$  is fundamental wind pressure;  $\beta_z$  is gust response coefficient;  $\mu_z$  is wind pressure height variation coefficient;  $\mu_s$  is the shape factor of wind load

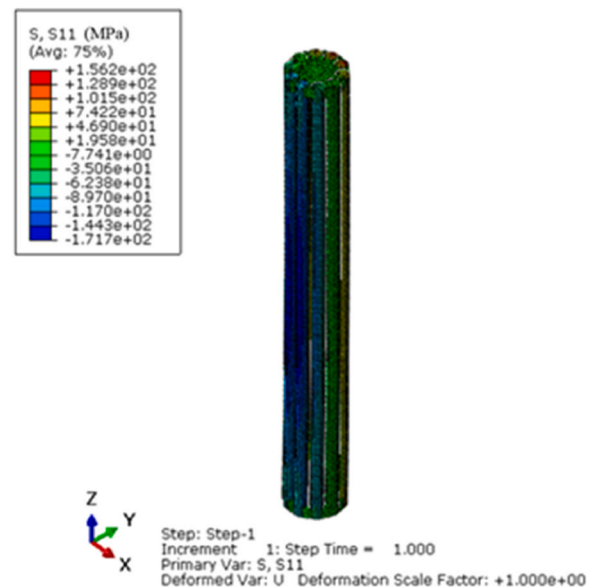
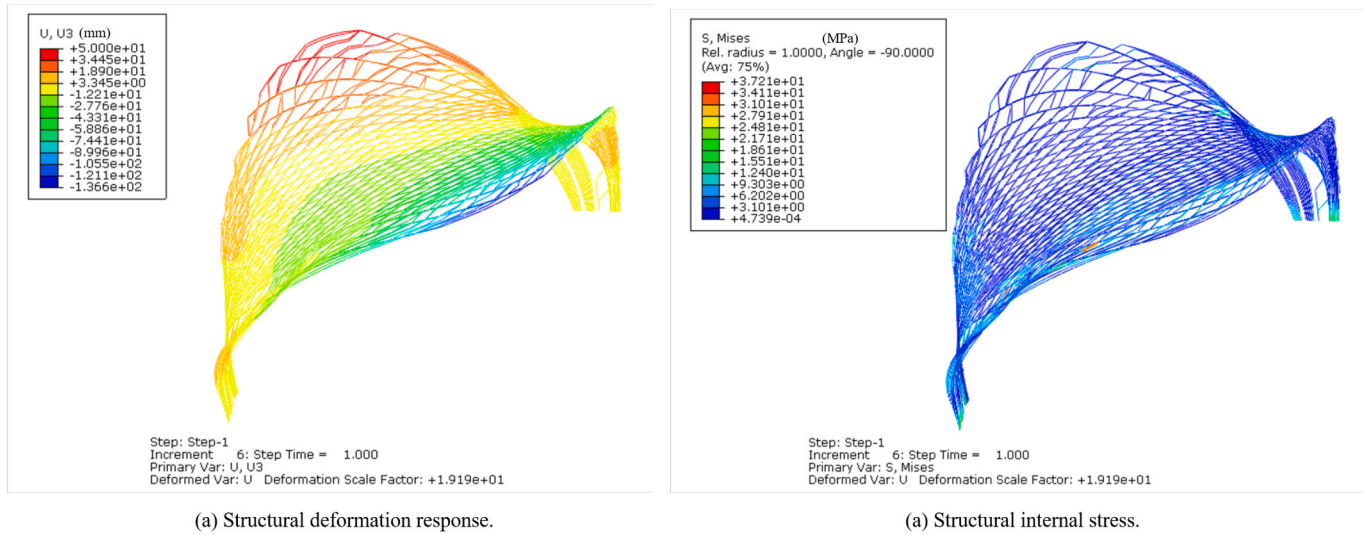
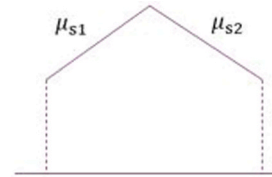


Fig. 14. The FEA result of bending at maximum curvature of bunched CFRP rods.

**Table 5**  
Value of shape factor of wind load  $\mu_s$ .

	$\mu_{s1}$	$\mu_{s2}$
$\leq 10^\circ$	-1.3	-0.7
$30^\circ$	+1.6	+0.4



**Fig. 15.** The FEA results of wind load effect.

selected by Table 5. The ground roughness category shall be C (urban areas with dense buildings). The overlap area of components was not considered. Consequently, the FEA result is conservative.

$$w_k = \beta_z \mu_s \mu_z w_0 \tag{16}$$

The deformation and stress of the structure under wind load are shown in Fig. 15. The maximum deformation of the structure under the most unfavorable wind load condition was 136.6 mm, which was less than 1/200 of the maximum structural span, fulfilling the safety requirements in load code for the design of building structures (GB50009–2012).

For the internal stress of the structure, the maximum stress was 37.2 MPa (taking Mises stress as a reference), which was still far less than the ultimate strength of CFRP material after superimposing the initial stress of the bending of the component about 400 MPa.

In summary, under the effect of wind load, the material strength and structural displacement can both meet the safety requirements.

### 5.2.3. Force analysis of joints

Since the focus of this paper is bending-active and self-shaping concepts, the stress state and mechanical properties of joints are briefly analyzed here. On the one hand, components in L0 and L1 layers are self-shaping, allowing them to bend into the designed shape without the restraint among components. Hence, for the first joint, there is essentially no force transfer. On the other hand, one side of the L2 layer components is inserted into the base, while the other end is overlapped onto the edge components, resulting in the tee sleeve subjected to tension and shear forces. The equations for calculating the tensile and shear strength of joints are as shown in Eqs. (17) and (18), where  $f_t, f_v$  are the tensile and shear strength of steel, and  $A_t, A_v$  are the area of the weakest section of joint under tension and shear forces, and  $F_{t,max}, F_{v,max}$  are the maximum value of the joint's normal and shear force. Take the tee sleeve

under wind load as an example, it is obvious that its ultimate bearing capacity is much greater than the maximum load. Besides, the design of other joints is also conservative enough to meet structural safety requirements.

$$N = f_t A_t = 884\text{kN} > F_{t,max} = 19.1\text{kN} \tag{17}$$

$$V = f_v A_v = 571\text{kN} > F_{v,max} = 13.4\text{kN} \tag{18}$$

### 5.3. Structural construction process

As described in Section 2.1, the bunched CFRP rods are constructed by separation-to-integration construction method. That is, individual slender straight rods are bent to a certain initial curvature prior to assembly, and then threaded one by one through positioning holes of joints to form the entire structural components. The above process mainly consists of the following stages:

- Around 60 days for production, package and transportation of CFRP rods, and installation of steel supports.
- Scaffolding and installing structural components of L0 layer takes around five days.
- Installation of structural components of L2 layer, roughly takes five days.
- Installation of structural components of L1 layer, also takes about five days.
- It takes about ten days to paint fireproof and anti-UV coating and install light belts.

Since the structure mainly consists of CFRP rods and connecting joints, the required on-site installation time is relatively short.

## 6. Discussion

This paper primarily focuses on the bending-active and self-shaping concepts in structural construction. Bending-active concept involves bending straight or flat components without concern for the final shape, whereas the self-shaping concept emphasizes achieving a designed shape after bending. To address both concepts, a CFRP self-shaping system is proposed that bends straight components into pre-designed shapes. Slender CFRP rods are bent and connected to form structural components, enabling self-shaping construction of complex curved free-form spatial structures. To validate these processes, planar bending tests are conducted on a variable section CFRP rod, comparing the results with simulations based on large deformation theory and FEA. Additionally, a practical case study is presented, focusing on the construction of a saddle-shaped canopy to demonstrate the feasibility of the design method and self-shaping system. It is important to note the following considerations:

- In the form-finding method presented in this paper, the large deformation theory relies on knowledge of the boundary conditions and reaction forces of the component. However, when the internal force conditions at a specific location within the component are unknown, it becomes challenging to compute the deformation at that point using the large deformation theory alone. Therefore, the large deformation theory is often employed in conjunction with FEM to address practical engineering problems.
- Regarding the inverse form-finding method, the segmented calculation method is employed in this paper. Although this method has low computational complexity and is straightforward to implement, it cannot accurately achieve self-shaping, as the actual deformation shape can deviate from the designed curve. Future research aims to enhance the precision of the inverse form-finding process by employing machine learning methods based on Recurrent Neural Network, to be specific, Long Short-term Memory (LSTM).
- In the experimental section in this paper, the effectiveness of the large deformation theory and FEA is validated through bending tests. The coefficient of determination  $R^2$ , as mentioned in Section 4.2, indicates that the deviation between the FEA results and the experimental data is minimal, with an approach towards 1. Besides, the midspan coordinates obtained from the large deformation theory are generally in good agreement with the experimental results. The influence of self-weight on the component's deformation is negligible, as evidenced by the comparison of SR-0 and SR-2. However, it is important to note that the bending-active construction method introduces significant stress to the components during the bending process. Ai et al. conducted long-term tensile creep tests on CFRP cables, showing that they had a million-hour creep coefficient ranging from 6.1 % to 7.9 % at stress levels from  $0.3 f_u$  to  $0.7 f_u$  (where  $f_u$  represents the characteristic tensile strength) [33]. Therefore, the long-term creep effect of CFRP on the whole structure can be ignored because of its low creep coefficient.
- In the design demonstration of the saddle-shaped spatial structure, the individual GFRP rods are required to sequentially pass through connecting joints. As the number of joints increases, it becomes increasingly difficult to manually assemble the whole structure. Hence, it is imperative to further optimize the construction of joints to address this issue and facilitate the construction process. Besides, FEA on joints should be conducted to further ensure their safety in practical application.
- For the aforementioned spatial structure, wind load is the dominant dynamic excitation. Numerical results have validated that the sum of initial stress and maximum stress under the wind load is significantly lower than the ultimate strength of CFRP material, proving its safety. However, in addition to considering wind load, it is also necessary to evaluate its safety and reliability under other conditions such as earthquakes in future designs.

## 7. Conclusions

This paper introduces the construction of bunched CFRP rods that meets the variable cross-section requirements and the “separation-to-integration” construction process based on the bending-active concept. The following conclusions can be drawn from this research:

- The proposed bunched CFRP rods can serve as primary load-bearing elements for arch bridges, landscape structures (such as canopies, park pavilions, mosques), and large-span space structures (including museums, libraries, sports venues), making them well-suited for constructing large-scale curved surface structures. Due to the use of CFRP composite materials, these components offer advantages over traditional structures, including lightweight, high design flexibility, and low maintenance requirements.
- The form-finding method based on large deformation theory and FEA is effective in determining the deformed shape of the components under known conditions of boundary constraints, external loading, and sectional forms. This method offers benefits such as small errors and high reliability.
- The inverse form-finding method based on segmented solutions enables efficient determination of the sectional forms of components, given the expected shape and considering the boundary constraints and external loading conditions. However, this method exhibits larger errors due to the sudden discontinuity in the cross-section.
- The results of the component bending tests align well with the theoretical results, confirming the effectiveness of the form-finding methods. Additionally, the experimental findings indicate that achieving high curvatures in specific areas of the component cannot be solely accomplished by adjusting stiffness. Therefore, sleeve construction can be employed to achieve the desired effects.
- Through static and dynamic load analyses, the safety and reliability of the saddle-shaped spatial structure designed in this study have been preliminarily validated. Furthermore, the effectiveness of the proposed bunched CFRP rods and the “separation-to-integration” construction method has been verified.

Conclusively, the proposed system offers several advantages: strong designability, low transportation cost, rapid construction, polished appearance, and low maintenance requirements. Future research will prioritize achieving high-precision inverse form-finding processes through LSTM, optimizing the construction of connecting joints, and studying long-term properties of the components.

### CRediT authorship contribution statement

**Peng Feng:** Writing – review & editing, Supervision, Resources, Project administration, Conceptualization. **Jiacheng Zhao:** Writing – original draft, Methodology, Investigation, Formal analysis. **Qinyu Wang:** Writing – review & editing, Visualization. **Jiaqi Zhai:** Methodology, Data curation. **Peizhao Zhou:** Writing – review & editing, Validation.

### Declaration of Competing Interest

The authors declare that they have no known competing financial interests or personal relationships that could have appeared to influence the work reported in this paper.

### Data Availability

Data will be made available on request.

### Acknowledgments

This research was supported by the National Key R&D Program of

China (2021YFB3704400, the New Cornerstone Science Foundation through the XPLOER PRIZE, and Guoqiang Institute, Tsinghua University (2021GQG1001).

## References

- [1] Shahbazi Y, Ghofrani M, Pedrammehr S. Aesthetic assessment of free-form space structures using machine learning based on the expert's experiences. *Buildings* 2023;13(10):2508.
- [2] Lienhard J, Knippers J. Considerations on the scaling of bending-active structures. *Int J Space Struct* 2013;28.
- [3] O. Frei, B. Burkhardt, M.B.ächer, *Multihalle Mannheim, Institut für leichte Flächentragwerke*, Stuttgart, Baden-Württemberg, 1978.
- [4] Jiang T, Song Y, Ning N. Bending-active gridshells:a review. *Spat Struct* 2021;27(2):24–33.
- [5] D. Wendland, *Model-based formfinding processes: Free forms in structural and architectural design*, (2008).
- [6] L.K.-L. Vaultot, *Form-finding of elastic gridshells*, Massachusetts Institute of Technology, 2016.
- [7] McQuaid Matilda, Otto F, Ban Shigeru. Illustrated ed.. Phaidon Press; 2006.
- [8] Harris R, Romer J, Kelly O, Johnson S. Design and construction of the Downland Gridshell. *Build Res Inf* 2003;31(6):427–54.
- [9] Harris R, Haskins S, Roynon J. The Savill Garden gridshell: design and construction. *Struct Eng* 2008;86(17):27–34.
- [10] Chilton J, Tang G. *Timber gridshells: architecture, structure and craft*. Routledge; 2016.
- [11] Puystiens S, Van Craenenbroeck M, Van Hemelrijck D, Van Paepegem W, Mollaert M, De Laet L. Implementation of bending-active elements in kinematic form-active structures – Part I: Design of a representative case study. *Compos Struct* 2019;216:436–48.
- [12] Puystiens S, Van Craenenbroeck M, Van Hemelrijck D, Van Paepegem W, Mollaert M, De Laet L. Implementation of bending-active elements in kinematic form-active structures – Part II: experimental verification. *Compos Struct* 2019; 213:1–13.
- [13] Kriklenko E. Complex bending-active structures from continuous flexible planar sheets or a hybrid structure introducing the use of spacer fabrics. *ARCHITECTURAL Eng Des Manag* 2021;17(3-4):242–63.
- [14] J. Bellmann, K. Bletzinger, E. Onate, B. Kroplin, *Active bending starting on curved architectural shape, vii international conference on textile composites and inflatable structures (structural membranes 2017)*, 2017, pp. 265–274.
- [15] Sonntag D, Bechert S, Knippers J. Biomimetic timber shells made of bending-active segments. *Int J Space Struct* 2017;32(3-4):149–59.
- [16] Fleischmann M, Knippers J, Lienhard J, Menges A, Schleicher S. Material behaviour: embedding physical properties in computational design processes. *Archit Des* 2012;82(2):44–51.
- [17] Kotelnikova-Weiler N, Douthe C, Hernandez EL, Baverel O, Gengnagel C, Caron J-F. Materials for actively-bent structures. *Int J Space Struct* 2013;28(3-4):229–40.
- [18] Ai PC, Feng P, Lin HW, Zhu PC, Ding GZ. Novel self-anchored CFRP cable system: concept and anchorage behavior. *Compos Struct* 2021;263.
- [19] Ding G, Feng P, Wang Y, Ai P. Novel pre-clamp lap joint for CFRP plates: design and experimental study. *Compos Struct* 2022;302.
- [20] Huang W, Wu C, Huang J. A weaving structure for design & construction of organic geometry. *Proc IASS Annu Symp, Vol 2017, Int Assoc Shell Spat Struct (IASS) 2017: 1–8.*
- [21] Dai J-G, Bai Y-L, Teng JG. Behavior and modeling of concrete confined with FRP composites of large deformability. *J Compos Constr* 2011;15(6):963–73.
- [22] Tayeb F, Caron JF, Baverel O, Du Peloux L. Stability and robustness of a 300 m2 composite gridshell structure. *Constr Build Mater* 2013;49:926–38.
- [23] Baverel O, Caron J-F, Tayeb F, Du Peloux L. Gridshells in composite materials: construction of a 300 m2 forum for the holidays' festival in Paris. *Struct Eng Int* 2012;22(3):408–14.
- [24] Nicholas P, Hernandez E, Gengnagel C. The Faraday Pavilion: activating bending in the design and analysis of an elastic gridshell. *Symp Simul ARCHITECTURE URBAN Des (SIMAUD 2013) - 2013 SPRING Simul MULTI-Conf (SPRINGSIM' 13) 2013;45(8):154–61.*
- [25] W.X. Huang, Y.Q. Sun, J.Y. Zhou, H.Y. Pan, *MOBIUS Pavilion: A Double-Layer Grid Shell Combined with Ice Based on Bending-active Weaving Structure*, IASS 60th anniversary symposium (iass symposium 2019) - 9th international conference on textile composites and inflatable structures (structural membranes 2019), 2019, pp. 1910–1915.
- [26] Levien R. *The elastica: a mathematical history*, 70. Electrical Engineering and Computer Sciences University of California at Berkeley; 2008.
- [27] Lienhard J. *Bending-active structures: form-finding strategies using elastic deformation in static and kinematic systems and the structural potentials therein*. University of Stuttgart; 2014.
- [28] Fertis DG. *Nonlinear structural engineering*. Heidelberg: Springer; 2006.
- [29] Oreilly OM. A properly invariant-theory of small deformations superposed on large deformations of an elastic rod. *J Elast* 1995;39(2):97–131.
- [30] Pinkall U, Polthier K. Computing Discrete Minimal Surfaces and Their Conjugates. *Exp Math* 1993;2(1):15–36.
- [31] Floater MS. Parametrization and smooth approximation of surface triangulations. *Comput Aided Geom Des* 1997;14(3):231–50.
- [32] P. Hu, L. Chen, J. Wang, K. Tang, *Boundary-conformed tool path generation based on global reparametrization*, 2015 14th International Conference on Computer-Aided Design and Computer Graphics (CAD/Graphics), IEEE, 2015, pp. 165–172.
- [33] Ai P, Ding G, Li Z, Feng P. Long-term creep behavior of novel self-anchored CFRP cable system. *Compos Struct* 2024:117965.